JCE

Journal Of
Civil Engineering
ISSN 2086 - 1206 E-ISSN 2579 - 9029

Finite element modeling of square confined concrete columns with stainless steel and carbon steel under concentric load

Venesia S. Samallo[a*], Bambang Piscesa[a], Heppy Kristijanto[a]

Correspondence

[a]Civil Engineering Department, Institute of Technology Sepuluh Nopember, ITS Campus, Surabaya, East Surabaya 60111, Indonesia.

Corresponding author email adress: venesiasamallo27@gmail.com

Submitted : 06 February 2026
Revised : 27 February 2026
Accepted : 5 Maret 2026

Abstract

The use of conventional carbon steel in steel tube confined concrete (STCC) structures presents durability challenges, particularly in marine environments, due to corrosion susceptibility and high maintenance requirements. Stainless steel tube confined concrete (SSTCC) offers enhanced corrosion resistance and improved long-term performance compared to carbon steel tube confined concrete (CSTCC). This study aims to validate numerical simulations against experimental results by evaluating load–displacement and stress–strain responses, while considering the effects of surface contact sensitivity between the concrete core and steel tube, as well as initial imperfections within the shear band region. A three-dimensional nonlinear finite element analysis (3D-NLFEA) model was developed for square cross-section STCC columns. The numerical results demonstrate strong agreement with experimental data. The comparison of load–displacement curves shows an average discrepancy of 3.22%, while the stress–strain responses exhibit an average difference of 5.00%. Improved correlation was achieved by incorporating a 10% material reduction to represent initial imperfections in the shear band region and calibrated surface contact parameters, including a cohesive strength of 0.7 MPa, a uniaxial tensile strength of 1.0 MPa, and an internal friction angle of 15°. These findings confirm the capability of the proposed numerical model to accurately predict the structural behavior of square STCC columns and highlight the effectiveness of stainless steel confinement in enhancing structural performance.

Keywords

3D-NLFEA, Stainless steel, Carbon steel, Initial imperfection, Contact surface sensitivity

INTRODUCTION

To increasing the strength of concrete in structures in the marine environment, there are two methods commonly used, namely internal and external reinforcement. One of the method of external strengthening, known as Steel Tube Confined Concrete (STCC), which involves the use of steel tubes as concrete reinforcement. Reinforcement using STCC on column piers as external confinement provides advantages, such as higher compressive capacity due to the confining effect and better ductility [1][2][3][4]. CFST is a fairly popular external confinement that has been widely applied to structures and structures in the marine environment [5][6][7][8]. The main difference between STCC and Concrete-Filled Steel Tube (CFST) is that STCC in steel tubes does not carry axial loads directly, thereby reducing the risk of local buckling. When concrete and steel tubes are loaded simultaneously, the steel tubes will provide less confinement than specimens that are only loaded on the concrete core, so that the effectiveness of STCC on the steel tubes that restrain the concrete core is maximized. CFST is not effective in bridge structures due to connection difficulties, meanwhile STCC can be applied effectively in beam-column or column-foundation connections to avoid direct axial loads and facilitate implementation [9][10].

The use of conventional carbon steel in STCC causes problems such as corrosion, therefore the use of stainless steel material (SSTCC) is very suitable for structures in the marine environment. Although stainless steel material has high initial cost, its maintenance costs are low making it a cost-effective choice [11]. Stainless steel material is suitable for structures in marine environments due to its corrosion resistance, fire resistance, and also has an aesthetic appearance [12][13]. The combination of confinement with STCC and stainless steel material makes it a better choice of reinforcement, which has been done by several previous researchers [14][15]. The mechanical properties of stainless steel are more variable than carbon steel and STCC using stainless steel material shows a stress-strain relationship curve without yield areas compared to carbon steel [16][17].

Initial imperfection is an initial defect given to a column before loading, where initial imperfection can influence the behavior of the column under loading and is considered in modeling to predict more accurate results [18][19][20]. External confinement in concrete allow defects to occur, such as a very large shear band in a column leading to shear

failure. This occurs if the shear stress applied to the shear band area exceeds the shear capacity of the material. In the shear band area, uneven distributed shear can occur and lead to poor load redistribution and trigger failure [21]. The shear band area in STCC is an area that experiences shear with higher intensity so that there is a significant change in the stress distribution that occurs due to the applied pressure [22]. Failure in the shear band area can be caused by various factors, one of which is an improper assembly process which causes premature failure, such as the welding quality of the steel tube which affects the stress distribution and material properties, giving rise to residual stress [23]. Specimen modeling should take into account of initial imperfection in the shear band area so that the modeling results are closer to actual failure conditions.

Surface contact between concrete elements and steel tube elements in STCC which is a physical and mechanical connection, where in this case the concrete is reinforced with steel contained in the steel tube. Surface contact between two different material properties can cause surface sensitivity between elements in the form of higher slip when the two elements meet the interface when subjected to load, especially in concrete elements and steel tube elements. Modeling surface contact between concrete elements and steel tube elements using Mohr-Coloumb plasticity with Zero Thickness Element is one of the numerical modeling methods used in finite element analysis to represent the interface interaction between concrete and steel tubes in STCC. This modeling allows a more accurate simulation of the STCC behavior under loading by assuming the interaction effect between concrete and steel tubes to obtain better results [24]. Several previous studies carried out analyzes regarding the sensitivity of surface contact on concrete elements and steel tube elements [25].

Previous research regarding finite element modeling in STCC has been carried out by [26][27]. Experimental research on STCC comparing the use of steel tubes with stainless steel and carbon steel as confinement for concrete has been carried out by [14]. Numerical analysis using the 3D-NLFEA program has been carried out by several previous studies to simulate modelling [28][29][30]. The 3D-NLFEA program is a program developed by [31][32][33][34][35][36][37]. In this study, finite element analysis will be conducted to obtain load–displacement and stress–strain curves for validating the experimental results reported in [15], while considering initial imperfections and surface contact sensitivity. The STCC columns with square cross-sections will be modeled by varying the steel type, steel tube thickness, and concrete strength. For this purpose, the 3D-NLFEA package will be employed in the numerical simulations.

RESEARCH SIGNIFICANCE

This study investigates the behavior of square cross-section concrete columns confined by steel tubes made of stainless steel and carbon steel. The test specimens are subjected to concentric loading. The specimens are modeled using nonlinear finite element methods to generate load–displacement and stress–strain relationship curves, which are subsequently compared. The modeling is carried out using the 3D-NLFEA package, with SALOME employed as the pre-processor and ParaView as the post-processor. The analysis considers initial imperfection parameters in the shear band region, as well as surface contact sensitivity between the concrete and steel elements using zero-thickness elements. The modeling includes variations in steel type, steel tube thickness, and concrete strength.

METHODOLOGY

The research methodology begins with modeling square cross-section concrete column specimens confined by stainless steel tube confined concrete (SSTCC) and carbon steel tube confined concrete (CSTCC), which are validated against experimental results. The modeling process employs the 3D-NLFEA program, with SALOME used as the pre-processor and ParaView as the post-processor. Initial imperfection parameters and surface contact sensitivity are considered to validate the load–displacement and stress–strain relationship curves, along with specimen variations, including steel type, steel tube thickness, and concrete strength. A detailed explanation of the research methodology is presented in the following sections.

A. SPECIMEN GEOMETRY, MATERIAL PROPERTIES, AND 3D-MODELING

The geometric data and material properties of the concrete, steel tubes, and steel blocks were adopted from the experimental study reported in [15]. The specimens had a height (H) of 450 mm and a width/diameter (D) of 150 mm, resulting in a slenderness ratio of 3.0. The study considered variations in steel type (stainless steel and carbon steel), steel tube thickness (2, 3, and 4 mm), and concrete strength (25 and 32 MPa). A total of eight specimens were modeled, consisting of six SSTCC specimens and two CSTCC specimens. Carbon steel tubes were used for comparison, with thickness corresponding to the largest tube thickness. For each configuration, two identical specimens were prepared, denoted as a and b. The details of the SSTCC and CSTCC specimens are presented in Table 1.

Table 1 Detail Specimen of SSTCC and CSTCC

Specimen	Variation		
	Type	Concrete strength (f_c)	Steel Tube Thickness (t_D)
		MPa	mm
SS2N	Stainless	25	2
SS2H	Stainless	32	2
SS3N	Stainless	25	3
SS3H	Stainless	32	3
SS4N	Stainless	25	4
SS4H	Stainless	32	4
CS4N	Carbon	25	4
CS4H	Carbon	32	4

The material properties of the test specimens are based on variations of the concrete strength (normal strength 25 MPa and high strength 32 MPa), as shown in Table 2. The material properties of stainless steel and carbon steel for variations in tube thickness are shown in Table 3.

Table 2 Material Properties of Concrete

Strength grade	f_c (MPa)	E_c (MPa)	POS	Density (kg/m^3)
Normal strength	25	22612.12	0.2	2200
High strength	32	37388.33	0.2	2200

Table 3 Material Properties of Stainless Steel Tube and Carbon Steel Tube

Type	t_D (mm)	fy (MPa)	Es (GPa)	POS	Density (kg/m^3)
Stainless	2	335	193	0.283	8000
Stainless	3	401	193	0.283	8000
Stainless	4	406	193	0.283	8000
Carbon	4	325	200	0.26	7850
Carbon	4	282	200	0.26	7850

Figure 1 shows the geometry of square cross-section concrete column specimen confined by steel tube made of stainless steel (SSTCC) and carbon steel (CSTCC). The specimen loading is in the form of concentric axial compressive load subjected only to the concrete core and the steel tubes as concrete restraints. Steel blocks of 50 mm thick are installed on the top and bottom of the concrete with steel block material properties shown in Table 4.

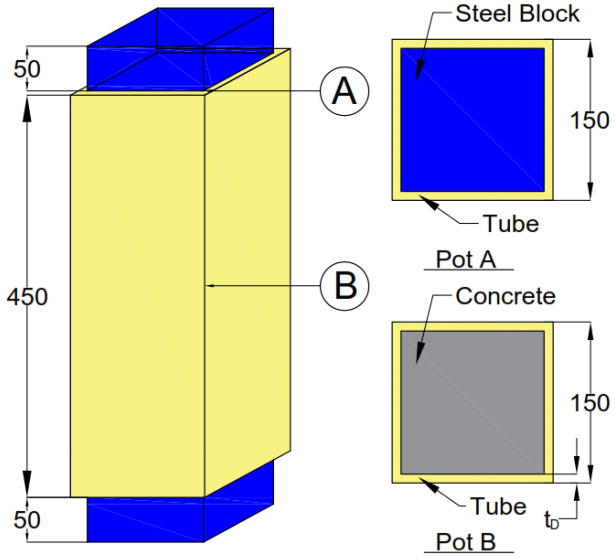

Figure 1 Specimen of Square Cross-section

Table 4 Material Properties of Steel Block

Notation	Steel Block
fy (MPa)	433
Es (GPa)	206
Poisson's ratio	0.3
Density (kg/m^3)	7850

The modeling of SSTCC and CSTCC specimens are using 3D-NLFEA program with pre-processor and post-processor using SALOME and ParaView.

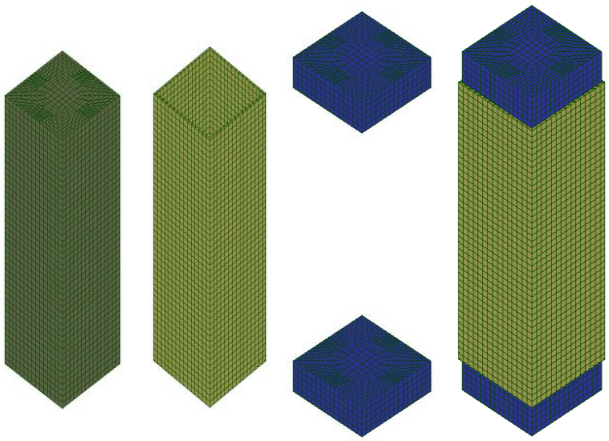

Figure 2 Specimen meshed model of SS4N in SALOME : (a) concrete, (b) tube, (c) steel block, (d) STCC

Figure 2 shows the specimen model in the SALOME program of the SS4N specimen, namely stainless steel type, square cross section, tube thickness 4 mm, and normal concrete strength which has the number of elements 13681 and the total number of nodes 20552. The boundary conditions are using displacement control with increments set to -0.01 mm at the top end, and at the bottom end set in all directions.

B. PARAMETER OF INITIAL IMPERFECTION IN SHEAR BAND AREA

Shear band areas will form in STCC columns where significant deformation occurs. This is because imperfections in the column cannot be avoided, therefore the imperfection parameters must be taken into account from the start to obtain more realistic results. Imperfection is a decrease in material in a shear band area that is systematically reduced to represent the initial imperfection that exists in the actual condition of the specimen [38]. The initial imperfection area of the shear band in the STCC column uses random material properties, namely the Box-Muller random number generator method which is also carried out by [20] which can be seen in equation 1.

$$f_{yi} = f_{ym} + \sigma_{f_y} \quad (1)$$

$$\sigma_{f_y} = \sqrt{2 \log\left(\frac{1}{x_1}\right)} \cos(2\pi x_2)$$

$$x_1 = rand(0,1) \; ; \quad x_2 = rand(0,1)$$

Where f_{yi} is the yield stress for the i-th mesh element, f_{ym} is the average yield stress, σ_{f_y} is the standard deviation of the average yield stress, x_1 and x_2 are random number generators varying from zero to one. The average values of yield strength are as follows:

$$f_{ym} = f_y + \alpha\, \sigma_{f_y} = f_y + \alpha \left(\Omega_{f_y} f_y\right) = \left(1 + \alpha\, \Omega_{f_y}\right) f_y$$

Where α is the standard deviation reflecting the probability of material failure of 5% so that the constant value for α is 1.64, Ω_{f_y} is the material variation coefficient.

The initial imperfection given in the shear band area is the material property that will be derived in the shear band

area which is implemented into the analysis model. The imperfections parameters inputted in the modeling using the 3D-NLFEA program are the thickness of the shear band (w) and the angle of inclination of the shear band (α) according to experimental conditions of 45º to 60º. Figure 3 shows a visualization of the failure mode of the SS4N specimen by taking into account the initial imperfection parameter in the shear band area.

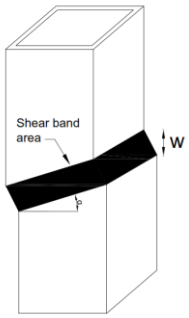

Figure 3 Visualization of imperfection in shear band area

C. PARAMETER OF SURFACE CONTACT SENSITIVITY

Sensitivity is defined by the shear stress capacity of the concrete–steel interface prior to slip, which depends on the friction coefficient between the two materials. The interface behavior is modeled using the Mohr–Coulomb plasticity model, which describes inelastic material behavior based on cohesion and friction angle governing shear resistance under effective normal stress. Zero thickness elements (ZTE) are employed to represent direct contact interaction without physical thickness. The application of the Mohr–Coulomb model with ZTE in STCC has been reported in [39] as expressed in Equation (2):

$$f = \tau_1^n + \tau_2^n - (c - \sigma_n \tan\phi)^n + (c - \xi \tan\phi)^n \quad (2)$$

Where τ_1 and τ_2 are the principal shear stresses, c is cohesion, ϕ is the friction angle, ξ is the bond strength (uniaxial tensile strength), and n is the elliptic curve control parameter (default = 2). In the 3D-NLFEA modeling, the ZTE parameters include cohesion strength, uniaxial tensile strength, and friction angle. The square cross-section specimen modeling in SALOME is shown in Figure 4.

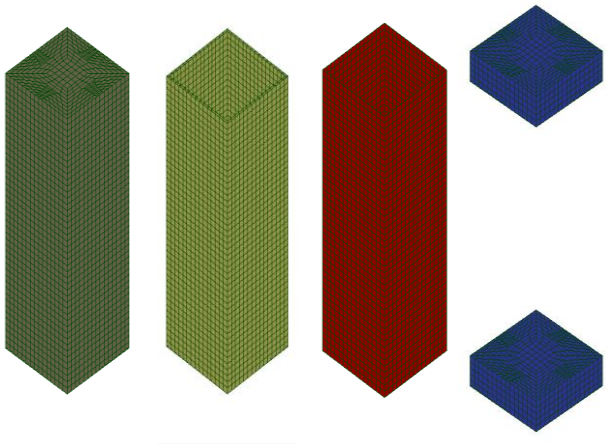

(a) (b) (c) (d)

Figure 4 Modeling square cross-section interface elements in SALOME: (a) concrete, (b) tube, (c) interface, (d) steel block

RESULTS AND DISCUSSIONS

Figures 5 to 13 present the load–displacement curves with variations in steel tube material, steel tube thickness, and concrete strength grade. Figure 5 shows the SS4N specimen for a comparison of load-displacement curves based on modeling results and experimental results without initial imperfections and zero thickness elements. A peak load of 1574.98 kN at a displacement of 3.86 mm is obtained, while based on experimental results a peak load of 704.48 kN at a displacement of 4.15 mm is obtained. Comparison of peak load based on modeling results and experimental results is 123.57 %.

Figure 6 shows a comparison of load-displacement relationship curves of SS4N specimens and is taking into account initial imperfections and surface contact sensitivity based on modeling results and experimental results. It can be seen that based on the modeling results of the SS4N specimen, a peak load of 722.56 kN at a displacement of 3.98 mm is obtained, while based on experimental results a peak load of 704.48 kN is obtained at a displacement of 4.07 mm. Comparison of peak load based on modeling results and experimental results is 2.57 %. It can be seen in Figure 7 that based on the modeling results of SS4H specimen, a peak load of 922.08 kN at a displacement of 4.22 mm is obtained, while based on experimental results a peak load of 942.83 kN is obtained at a displacement of 3.49 mm. Comparison of peak load based on modeling results and experimental results is 2.20 %.

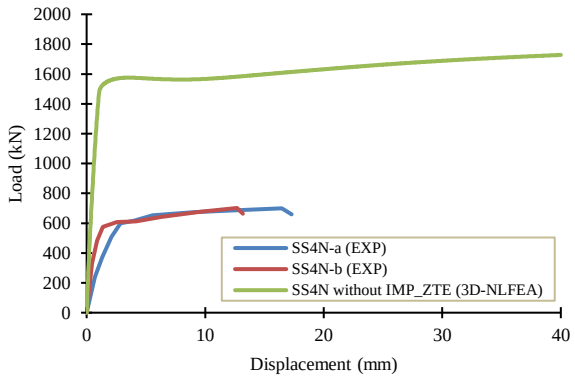

Figure 5 Comparison of experiment and modeling curve without imperfection and zero thickness element of SS4N

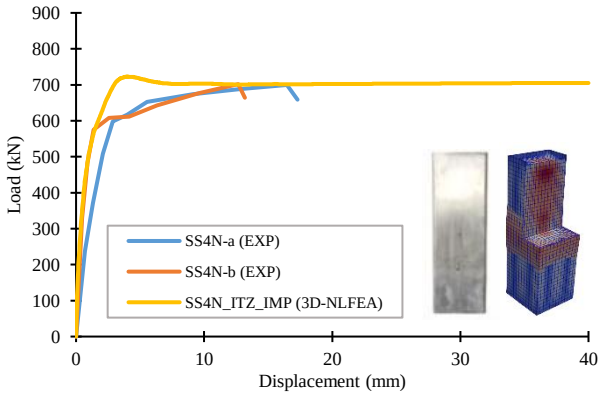

Figure 6 Comparison of experiment and modeling curve with imperfection and zero thickness element of SS4N

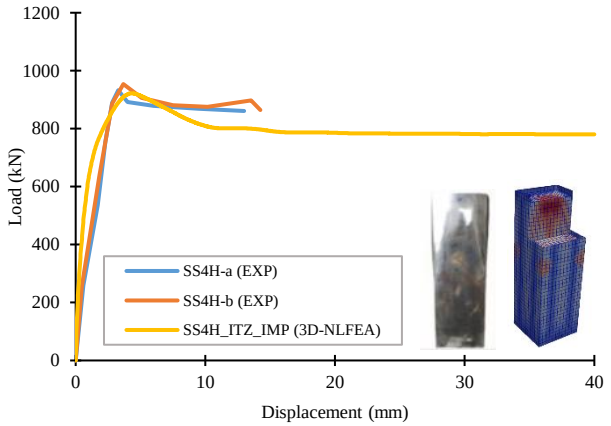

Figure 7 Comparison of experiment and modeling curve with imperfection and zero thickness element of SS4H

Figure 8 shows that based on the modeling results of SS3N specimen, a peak load of 577.07 kN at a displacement of 4.02 mm is obtained, while based on experimental results a peak load of 545.36 kN is obtained at a displacement of 2.41 mm. Comparison of peak load based on modeling results and experimental results is 5.81 %. As shown in Figure 9, it can be seen that based on the modeling results of SS3H specimen, a peak load of 837.75 kN at a displacement of 4.22 mm is obtained, while based on experimental results a peak load of 796.26 kN is obtained at a displacement of 2.09 mm. Comparison of peak load based on modeling results and experimental results is 5.21 %.

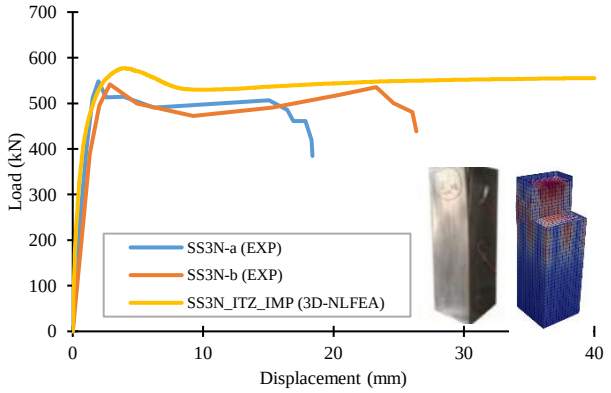

Figure 8 Comparison of experiment and modeling curve with imperfection and zero thickness element of SS3N

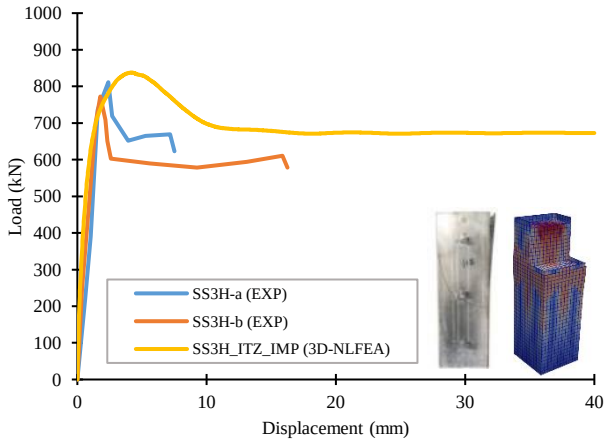

Figure 9 Comparison of experiment and modeling curve with imperfection and zero thickness element of SS3H

Figure 10 shows that based on the modeling results of SS2N specimen, a peak load of 560.44 kN at a displacement of 3.14 mm is obtained, while based on experimental results a peak load of 533.48 kN is obtained at a displacement of 2.09 mm. Comparison of peak load based on modeling results and experimental results is 5.05 %. Figure 11 shows that based on the modeling results of SS2H specimen, a peak load of 718.16 kN at a displacement of 2.48 mm is obtained, while based on experimental results a peak load of 750.7 kN is obtained at a displacement of 1.53 mm. Comparison of peak load based on modeling results and experimental results is 4.33 %.

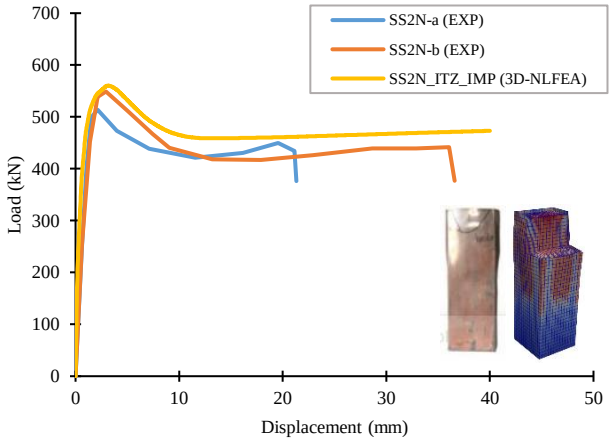

Figure 10 Comparison of experiment and modeling curve with imperfection and zero thickness element of SS2N

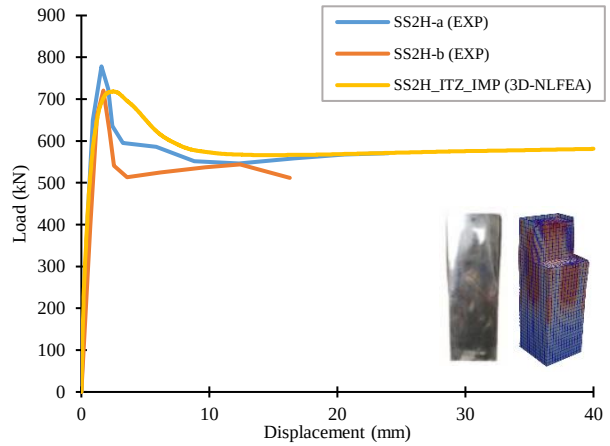

Figure 11 Comparison of experiment and modeling curve with imperfection and zero thickness element of SS2H

Figure 12 shows that based on the modeling results of CS4N specimen, a peak load of 667.98 kN at a displacement of 4.42 mm is obtained, while based on experimental results a peak load of 671.47 kN is obtained at a displacement of 4 mm. Comparison of peak load based on modeling results and experimental results is 0.52 %. Figure 13 shows that based on the modeling results of CS4H specimen, a peak load of 712.19 kN at a displacement of 3.24 mm is obtained, while based on experimental results a peak load of 711.74 kN is obtained at a displacement of 3.92 mm. Comparison of peak load based on modeling results and experimental results is 0.06%.

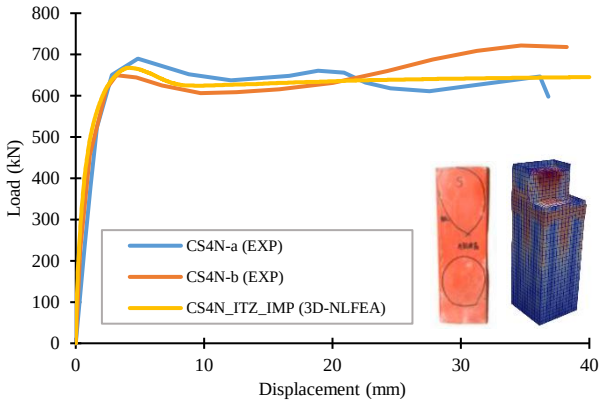

Figure 12. Comparison of experiment and modeling curve with imperfection and zero thickness element of CS4N

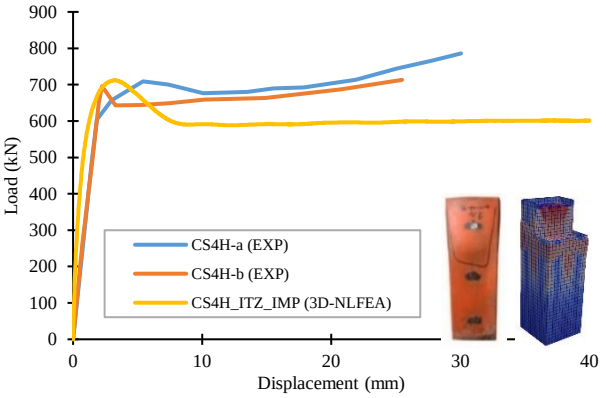

Figure 13. Comparison of experiment and modeling curve with imperfection and zero thickness element of CS4H

The analysis of initial imperfections in the shear band region (shear band thickness, w, and angle, α) is presented in Table 5. Random material variation indicates that a 10% imperfection produces load–displacement results closest to the experimental data. Surface contact sensitivity between concrete and steel (Table 6), evaluated through cohesion strength (C), uniaxial tensile strength (ξ), and friction angle (ϕ), shows that C = 0.7 MPa, ξ = 1.0 MPa, and ϕ = 15° provide the best agreement with experimental results.

The comparison of peak loads for SSTCC and CSTCC specimens (Table 7) demonstrates good correlation between numerical and experimental results. The SS4N specimen exhibits the highest peak load, with 722.56 kN (numerical) and 704.48 kN (experimental), resulting in a 2.57% difference. Increasing steel tube thickness (2, 3, and 4 mm) consistently enhances peak load capacity in both numerical and experimental results. Similarly, higher concrete strength leads to greater peak loads, as observed in SS4H compared to SS4N, while maintaining close agreement between numerical predictions and experimental data.

Table 5 Effect of Variation in imperfection to the predict peak load

w (mm)	α	Imperfect (%)	Peak Load (kN)	
			Experiment	3D-NLFEA
15	45	5	704.48	713.90
15	45	10	704.48	722.56
15	45	15	704.48	732.90

Table 6 Effect of Variation in c, ξ and ϕ to the predict peak load

C (MPa)	ξ (MPa)	ϕ (MPa)	Peak Load (kN)	
			Experiment	3D-NLFEA
0.6	1.0	15	704.48	688.50
0.7	1.0	15	704.48	722.56
0.8	1.0	15	704.48	761.38

Table 7 Comparison Peak Load of SSTCC and CSTCC

Specimen	Peak Load (kN)		Difference (%)
	Experiment	3D-NLFEA	
SS2N	533.48	560.44	5.05
SS2H	750.70	718.16	4.33
SS3N	545.36	577.07	5.81
SS3H	796.26	837.75	5.21
SS4N	704.48	722.56	2.57
SS4H	942.83	922.08	2.20
CS4N	671.47	667.98	0.52
CS4H	711.74	712.19	0.06

The 3D-NLFEA results show very close agreement with the experiments, with differences ranging from 0.06% to 5.81%. Overall, the numerical model reliably predicts the peak load capacity of both SSTCC and CSTCC specimens.

Figures 14 shows that based on the modeling results of the SS4N specimen, a peak stress of 47.47 MPa is obtained, while based on experimental results a peak stress of 45.40 MPa is obtained. The difference in peak stress between modeling and experimental results is 4.55%. Figure 15 shows that based on the modeling results of the SS4H specimen, a peak stress of 51.15 MPa is obtained, while based on experimental results a peak stress of 50.03 MPa is obtained. The difference in peak stress between modeling and experimental results is 2.24%.

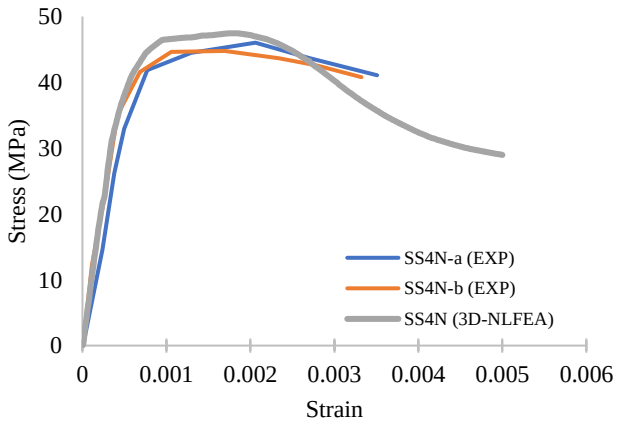

Figure 14. Stress–Strain Relationship of SS4N

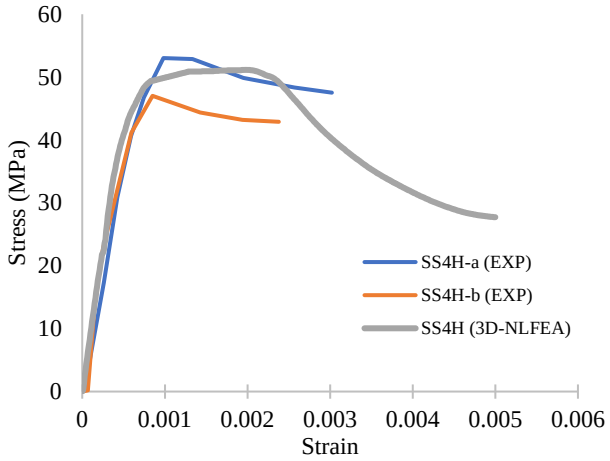

Figure 15. Stress–Strain Relationship of SS4H

Figures 16 shows that based on the modeling results of the SS3N specimen, a peak stress of 33.28 MPa is obtained, while based on experimental results a peak stress of 31.01 MPa is obtained. The difference in peak stress between modeling and experimental results is 7.32%. Figure 17 shows that based on the modeling results of the SS3H specimen, a peak stress of 41.30 MPa is obtained, while based on experimental results a peak stress of 38.39 MPa is obtained. The difference in peak stress between modeling and experimental results is 7.57%.

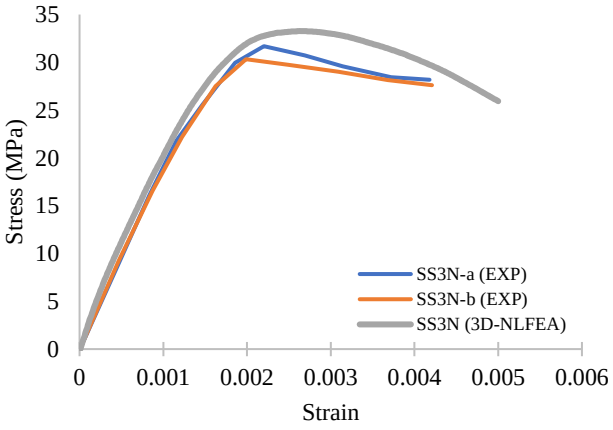

Figure 16. Stress–Strain Relationship of SS3N

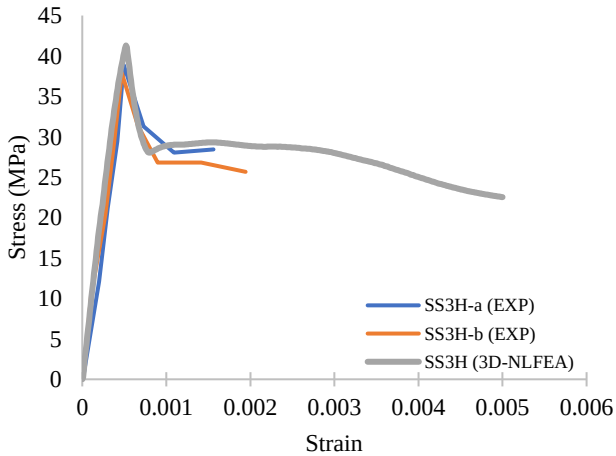

Figure 17. Stress–Strain Relationship of SS3H

Figures 18 shows that based on the modeling results of the SS2N specimen, a peak stress of 26.77 MPa is obtained, while based on experimental results a peak stress of 24.90 MPa is obtained. The difference in peak stress between modeling and experimental results is 7.53%.

Figure 19 shows that based on the modeling results of the SS2H specimen, a peak stress of 33.22 MPa is obtained, while based on experimental results a peak stress of 35.16 MPa is obtained. The difference in peak stress between modeling and experimental results is 5.52%.

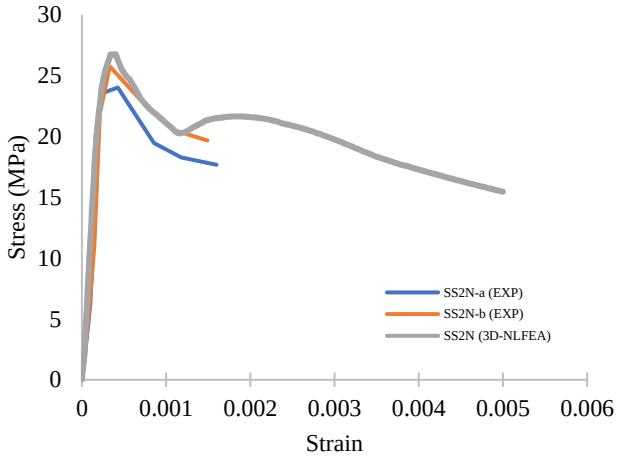

Figure 18. Stress–Strain Relationship of SS2N

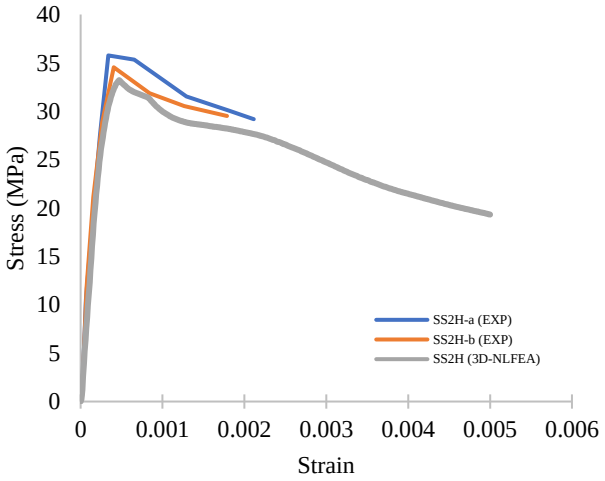

Figure 19. Stress–Strain Relationship of SS2H

Figure 20 shows that based on the modeling results of the CS4N specimen, a peak stress of 35.31 MPa is obtained, while based on experimental results a peak stress of 34.24 MPa is obtained. The difference in peak stress between modeling and experimental results is 3.11%. Figure 21 shows that based on the modeling results of the CS4H specimen, a peak stress of 51.00 MPa is obtained, while based on experimental results a peak stress of 49.93 MPa is obtained. The difference in peak stress between modeling and experimental results is 2.14%.

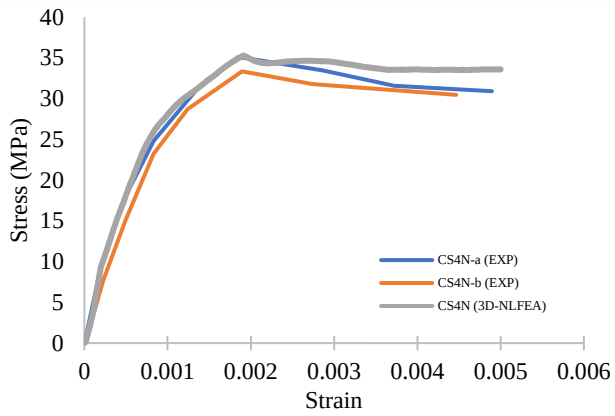

Figure 20. Stress–Strain Relationship of CS4N

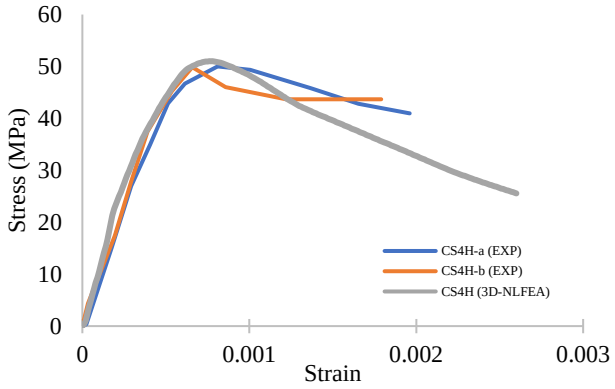

Figure 21. Stress–Strain Relationship of CS4H

Table 8 Comparison Peak Stress of SSTCC and CSTCC

Specimen	Peak Stress (MPa)		Difference (%)
	Experiment	3D-NLFEA	
SS2N	24.90	26.77	7.53
SS2H	35.16	33.22	5.52
SS3N	31.01	33.28	7.32
SS3H	38.39	41.30	7.57
334N	45.40	47.47	4.55
SS4H	50.03	51.15	2.24
CS4N	34.24	35.31	3.11
CS4H	49.93	51.00	2.14

Overall, the numerical results demonstrate good agreement with the experimental data for both SSTCC and CSTCC specimens in terms of peak stress prediction. Based on Table 8, the differences between experimental and 3D-NLFEA peak stress values range from 2.14% to 7.57%. The largest deviation is observed in SS3H (7.57%), followed by SS2N (7.53%) and SS3N (7.32%), while the smallest difference occurs in CS4H (2.14%). In general, the numerical predictions tend to be slightly higher than the corresponding experimental values. Nevertheless, the relatively small percentage differences indicate that the 3D-NLFEA model provides accurate and consistent predictions of the peak stress for both SSTCC and CSTCC specimens.

The failure modes obtained from the ParaView analysis (Figures 22–25) demonstrate that incorporating initial imperfections significantly improves the accuracy of the numerical predictions. Models without initial imperfections tend to overestimate the peak load and show a more uniform stress distribution, which does not fully represent the experimentally observed localized crushing and buckling. In contrast, the inclusion of shear band imperfections produces earlier strain localization and failure patterns that closely match the experimental results.

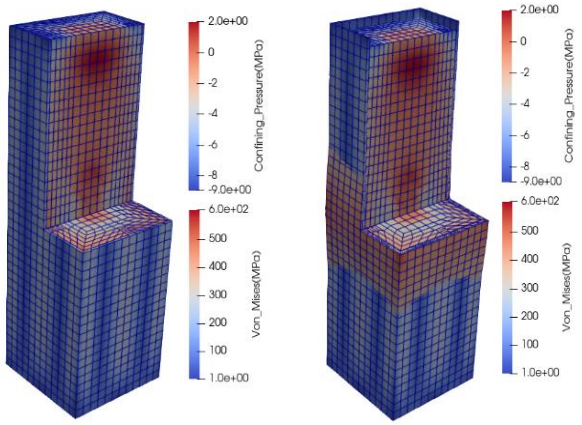

(a) (b)

Figure 22. SS4N Specimen with Imperfection and ZT: (a) without imperfection, (b) with imprefection

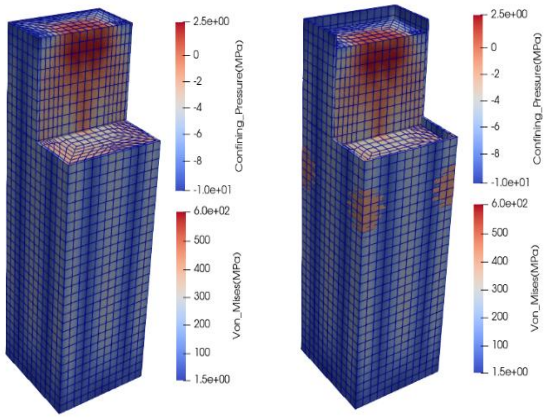

(a) (b)

Figure 23. SS4H Specimen with Imperfection and ZTE: (a) without imperfection, (b) with imprefection

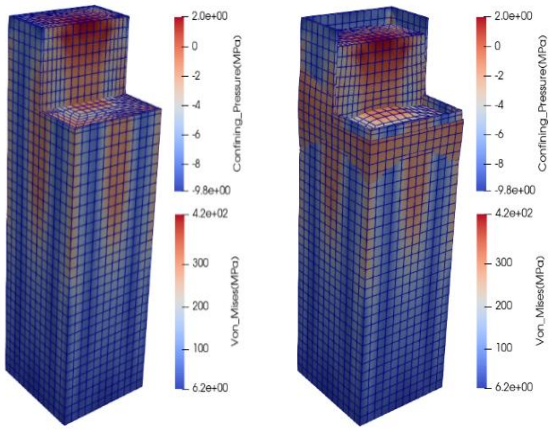

(a) (b)

Figure 24. CS4N Specimen with Imperfection and ZTE: (a) without imperfection, (b) with imprefection

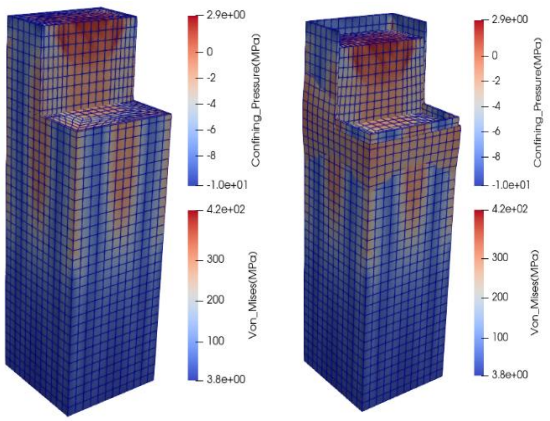

Figure 25. CS4H Specimen with Imperfection and ZTE: (a) without imperfection, (b) with imprefection

For the SS4N specimen, the initial imperfection was introduced at mid-height, while for SS4H, CS4N, and CS4H specimens, it was located near the upper end, consistent with the experimentally observed critical regions. The calibrated surface interaction between the concrete core and steel tube successfully captured the confinement mechanism, including concrete dilation and corresponding stress development in the steel tube. Overall, the modeling approach effectively reproduced both the deformation patterns and failure modes observed experimentally.

The research findings indicate that the 3D-NLFEA numerical model is capable of adequately representing the behavior of steel tube–confined concrete columns compared to the experimental results, particularly in the elastic stage up to near the peak load. The load–displacement and stress–strain curves exhibit consistent trends, with relatively small deviations in peak load and peak stress values. Increasing the thickness of the steel tube significantly enhances both the load capacity and peak stress due to the increased confinement pressure applied to the concrete core. Furthermore, the use of higher-strength concrete results in greater compressive capacity; however, the post-peak response tends to become steeper due to stress concentration at the corners of the square cross-section. In terms of material type, specimens confined with stainless steel tubes demonstrate higher peak capacity compared to those with carbon steel tubes, indicating a more effective confinement mechanism in enhancing the compressive strength of the composite system.

Regarding the initial compressive stiffness, the analysis shows that the influence of steel tube confinement during the early elastic stage is relatively insignificant. The slope of the curve in the initial linear phase is nearly similar across all specimen variations, whether confined with stainless steel or carbon steel tubes. This finding suggests that the initial response of the system is predominantly governed by the elastic modulus of the concrete core, while the confinement effect becomes more pronounced only after significant lateral expansion of the concrete occurs in the nonlinear stage. Therefore, the primary contribution of the steel tube lies in improving peak capacity, ductility, and post-peak stability rather than increasing the initial elastic stiffness.

CONCLUSIONS

This study investigated the structural behavior of square cross-section concrete columns confined with stainless steel and carbon steel tubes using a three-dimensional nonlinear finite element analysis (3D-NLFEA) framework. The model incorporated initial geometric imperfections within the shear band region and surface contact sensitivity parameters to improve predictive accuracy. Numerical simulations conducted without accounting for initial imperfections resulted in an overestimation of peak load compared to experimental findings. In contrast, the inclusion of initial imperfections led to significantly improved correlation, accurately capturing both the experimental load–deformation response and the observed failure mechanisms.

The parametric investigation identified the optimal shear band configuration as a thickness of 15 mm and an inclination angle of 45°, combined with a 10% reduction in concrete compressive strength and steel yield strength to represent material imperfections. For surface contact modeling, the most reliable agreement with experimental results was achieved using a cohesion strength of 0.7 MPa, a uniaxial tensile strength of 1.0 MPa, and a friction angle of 15°. Quantitative comparison demonstrated strong consistency between numerical and experimental outcomes, with differences of 3.22% in load–displacement responses and 5.00% in stress–strain behavior, while peak load discrepancies remained below 6% across all specimens. The findings further confirm that stainless steel confinement provides higher peak load capacity than carbon steel confinement. Moreover, increasing steel tube thickness and concrete compressive strength consistently enhances the ultimate load-carrying capacity of the composite column system.

REFERENCES

[1] H. Qi, L. Guo, J. Liu, D. Gan, and S. Zhang, “Axial load behavior and strength of tubed steel reinforced-concrete (SRC) stub columns,” *Thin-Walled Struct.*, vol. 49, no. 9, pp. 1141–1150, 2011, doi: 10.1016/j.tws.2011.04.006.

[2] A. Le Hoang and E. Fehling, “Numerical study of circular steel tube confined concrete (STCC) stub columns,” *J. Constr. Steel Res.*, vol. 136, pp. 238–255, 2017, doi: 10.1016/j.jcsr.2017.05.020.

[3] A. Haghinejad and M. Nematzadeh, “Three-dimensional finite element analysis of compressive behavior of circular steel tube-confined concrete stub columns by new confinement relationships,” *Lat. Am. J. Solids Struct.*, vol. 13, no. 5, pp. 916–944, 2016, doi: 10.1590/1679-78252631.

[4] J. Liu, Y. Teng, Y. Zhang, X. Wang, and Y. F. Chen, “Axial stress-strain behavior of high-strength concrete confined by circular thin-walled steel tubes,” *Constr. Build. Mater.*, vol. 177, pp. 366–377, 2018, doi: 10.1016/j.conbuildmat.2018.05.021.

[5] T. Kitada, “Ultimate strength and ductility of state-of-the-art concrete-filled steel bridge piers in Japan,” *Eng. Struct.*, vol. 20, pp. 347–354, 1998, doi: 10.1016/S0141-0296(97)00026-6.

[6] C. W. Roeder, M. T. Stephens, and D. E. Lehman, "Concrete Filled Steel Tubes for Bridge Pier and Foundation Construction," *Int. J. Steel Struct.*, vol. 18, no. 1, pp. 39–49, 2018, doi: 10.1007/s13296-018-0304-7.

[7] D. Saini and B. Shafei, "Performance of Concrete-Filled Steel Tube Bridge Columns Subjected to Vehicle Collision," *J. Bridg. Eng.*, vol. 24, no. 8, pp. 1–13, 2019, doi: 10.1061/(asce)be.1943-5592.0001439.

[8] M. Johansson and K. Gylltoft, "Mechanical Behavior of Circular Steel–Concrete Composite Stub Columns," *J. Struct. Eng.*, vol. 128, no. 8, pp. 1073–1081, 2002, doi: 10.1061/(asce)0733-9445(2002)128:8(1073).

[9] J. Liu and X. Zhou, "Behavior and strength of tubed RC stub columns under axial compression," *J. Constr. Steel Res.*, vol. 66, no. 1, pp. 28–36, 2010, doi: 10.1016/j.jcsr.2009.08.006.

[10] H. Wang, X. Zhou, J. Liu, X. Wang, and Y. F. Chen, "Seismic behavior of steel tube confined reinforced concrete double-column bridge bents," *J. Constr. Steel Res.*, vol. 166, pp. 1–11, 2020, doi: 10.1016/j.jcsr.2019.105919.

[11] H. Dewanbabee and S. Das, "Structural Behavior of Corroded Steel Pipes Subject to Axial Compression and Internal Pressure: Experimental Study," *J. Struct. Eng.*, vol. 139, no. 1, pp. 57–65, 2013, doi: 10.1061/(asce)st.1943-541x.0000596.

[12] H. Lu, L.-H. Han, and X.-L. Zhao, "Fire performance of self-consolidating concrete filled double skin steel tubular columns: Experiments," *Fire Saf. J.*, vol. 45, no. 2, pp. 106–115, 2010, doi: 10.1016/j.firesaf.2009.12.001.

[13] Z. Tao, B. Uy, F. Y. Liao, and L. H. Han, "Nonlinear analysis of concrete-filled square stainless steel stub columns under axial compression," *J. Constr. Steel Res.*, vol. 67, no. 11, pp. 1719–1732, 2011, doi: 10.1016/j.jcsr.2011.04.012.

[14] L. Guo, Y. Liu, F. Fu, and H. Huang, "Behavior of axially loaded circular stainless steel tube confined concrete stub columns," *Thin-Walled Struct.*, vol. 139, pp. 66–76, 2019, doi: 10.1016/j.tws.2019.02.014.

[15] Q. Qiyun, Y. Zhaoyuan, and C. Wanlin, "Axial compressive behavior of stainless steel tube confined concrete column piers," *Mar. Struct.*, vol. 78, pp. 1–25, 2021, doi: 10.1016/j.marstruc.2021.103021.

[16] E. Ellobody and B. Young, "Design and behaviour of concrete-filled cold-formed stainless steel tube columns," *Eng. Struct.*, vol. 28, no. 5, pp. 716–728, 2006, doi: 10.1016/j.engstruct.2005.09.023.

[17] M. Dundu, "Evolution of stress–strain models of stainless steel in structural engineering applications," *Constr. Build. Mater.*, vol. 165, pp. 413–423, 2018, doi: 10.1016/j.conbuildmat.2018.01.008.

[18] P. S. Harvey and T. M. N. Cain, "Buckling of elastic columns with initial imperfections and load eccentricity," *Structures*, vol. 23, pp. 660–664, 2020, doi: 10.1016/j.istruc.2019.09.021.

[19] A. M. Girão Coelho, P. D. Simão, and M. A. Wadee, "Imperfection sensitivity of column instability revisited," *J. Constr. Steel Res.*, vol. 90, pp. 265–282, 2013, doi: 10.1016/j.jcsr.2013.08.006.

[20] H. Kristijanto, B. Piscesa, F. Faimun, D. Iranata, and P. Suprobo, "Shear Buckling Analysis of Corrugated Web Steel Plate Girder with Random Material Properties," *Open Civ. Eng. J.*, vol. 16, no. 1, pp. 1–13, 2022, doi: 10.2174/18741495-v16-e2208050.

[21] L.-H. Han, Y. Ye, and F.-Y. Liao, "Effects of Core Concrete Initial Imperfection on Performance of Eccentrically Loaded CFST Columns," *J. Struct. Eng.*, vol. 142, no. 12, pp. 1–13, 2016, doi: 10.1061/(asce)st.1943-541x.0001604.

[22] M. E. Torki and A. A. Benzerga, "A mechanism of failure in shear bands," *Extrem. Mech. Lett.*, vol. 23, pp. 1–8, 2018, doi: 10.1016/j.eml.2018.06.008.

[23] Y. Ye, S. J. Zhang, L. H. Han, and Y. Liu, "Square concrete-filled stainless steel/carbon steel bimetallic tubular stub columns under axial compression," *J. Constr. Steel Res.*, vol. 146, pp. 49–62, 2018, doi: 10.1016/j.jcsr.2018.03.015.

[24] D. A. Moran, C. P. Pantelides, and L. D. Reaveley, "Mohr-coulomb model for rectangular and square FRP-confined concrete," *Compos. Struct.*, vol. 209, pp. 889–904, 2019, doi: 10.1016/j.compstruct.2018.11.024.

[25] D. H. Nguyen, W. K. Hong, H. J. Ko, and S. K. Kim, "Finite element model for the interface between steel and concrete of CFST (concrete-filled steel tube)," *Eng. Struct.*, vol. 185, pp. 141–158, 2019, doi: 10.1016/j.engstruct.2019.01.068.

[26] M. F. Hassanein, A. Y. Hamed, Y.-B. Shao, and N. Silvestre, "Confinement-based direct design of circular steel tube confined concrete (STCC) short columns," *J. Constr. Steel Res.*, vol. 204, pp. 1–14, 2023, doi: 10.1016/j.jcsr.2023.107871.

[27] Q. Yu, Z. Tao, W. Liu, and Z. B. Chen, "Analysis and calculations of steel tube confined concrete (STCC) stub columns," *J. Constr. Steel Res.*, vol. 66, no. 1, pp. 53–64, 2010, doi: 10.1016/j.jcsr.2009.08.003.

[28] S. I. Yansiku, B. Piscesa, and P. Suprobo, "Numerical Study on Discrete Confinement of Circular RC Column Subjected to Eccentric Load," *Open Civ. Eng. J.*, vol. 17, no. 1, pp. 1–8, 2023, doi: 10.2174/0118741495266900230925114616.

[29] S. I. Yansiku, B. Piscesa, and P. Suprobo, "Numerical Study on Slender Circular Reinforced Concrete Column Clamped with Steel Sheet," in *IOP Conference Series: Earth and Environmental Science*, 2023, vol. 1244, no. 1, pp. 1–10. doi: 10.1088/1755-1315/1244/1/012002.

[30] A. B. Christianto, B. Piscesa, M. M. Attard, Faimun, and P. Aji, "3D Finite element modeling of circular reinforced concrete column confined with CFRP under different eccentric loads," *IOP Conf. Ser. Mater. Sci. Eng.*, vol. 930, no. 1, pp. 1–9, 2020, doi: 10.1088/1757-899X/930/1/012047.

[31] B. Piscesa, M. Attard, A. K. Samani, and P. Suprobo, "Numerical Investigation on The

Behavior of Concrete-Filled-Steel-Tube Column under Eccentric Loading," in *The Third International Conference on Civil Engineering Research (ICCER)*, 2017, pp. 1–6.

[32] B. Piscesa, M. M. Attard, D. Prasetya, and A. K. Samani, "Modeling cover spalling behavior in high strength reinforced concrete columns using a plasticity-fracture model," *Eng. Struct.*, vol. 196, pp. 1–19, 2019, doi: 10.1016/j.engstruct.2019.109336.

[33] B. Piscesa, M. M. Attard, and A. K. Samani, "3D Finite element modeling of circular reinforced concrete columns confined with FRP using a plasticity based formulation," *Compos. Struct.*, vol. 194, pp. 478–493, 2018, doi: 10.1016/j.compstruct.2018.04.039.

[34] B. Piscesa, M. M. Attard, and A. K. Samani, "A lateral strain plasticity model for FRP confined concrete," *Compos. Struct.*, vol. 158, pp. 160–174, 2016, doi: 10.1016/j.compstruct.2016.09.028.

[35] B. Piscesa, M. M. Attard, and A. K. Samani, "Plastic dilation rate characteristic of concrete confined with steel tube," *Proc. 14th Int. Conf. Comput. Plast. - Fundam. Appl. COMPLAS 2017*, pp. 436–446, 2017.

[36] B. Piscesa, M. M. Attard, and A. K. Samani, "Three-dimensional Finite Element Analysis of Circular Reinforced Concrete Column Confined with FRP using Plasticity Model," *Procedia Eng.*, vol. 171, pp. 847–856, 2017, doi: 10.1016/j.proeng.2017.01.377.

[37] B. Piscesa, M. M. Attard, A. K. Samani, and S. Tangaramvong, "Plasticity constitutive model for stress-strain relationship of confined concrete," *ACI Struct. J.*, vol. 114, no. 2, pp. 361–371, 2017, doi: 10.14359/51689428.

[38] G. T. R. Smith, "The effect of initial imperfections on the strength of thin-walled box columns," *Int. J. Mech. Sci.*, vol. 13, no. 11, pp. 911–925, 1971, doi: 10.1016/0020-7403(71)90077-4.

[39] A. H. Yudhanto, B. Piscesa, M. M. Attard, B. Suswanto, and P. Suprobo, "Finite element modeling of concrete confined with circular thin-walled steel sheet," in *E3S Web of Conferences*, 2020, vol. 156, pp. 1–6. doi: 10.1051/e3sconf/202015605009.